

AN IMPRINT OF MOLECULAR CLOUD MAGNETIZATION IN THE MORPHOLOGY OF THE DUST POLARIZED EMISSION

J.D. SOLER¹, P. HENNEBELLE², P.G. MARTIN³, M.-A. MIVILLE-DESCHÊNES^{3,4}, C.B. NETTERFIELD^{1,5}, AND L.M. FISSEL¹

Submitted to ApJ, 2013 March 5

ABSTRACT

We describe a morphological imprint of magnetization found when considering the relative orientation of the magnetic field direction with respect to the density structures in simulated turbulent molecular clouds. This imprint was found using the Histogram of Relative Orientation (HRO): a new technique that utilizes the gradient to characterize the directionality of the density and column density structures on multiple scales. We present results of the HRO analysis applied to three models of molecular clouds in which the initial magnetic field strength is varied, but an identical initial turbulent velocity field is introduced, which subsequently decays. The HRO analysis was applied to the simulated data cubes and mock-observations of the simulations produced by integrating the data cube along particular lines of sight. In the 3D analysis we describe the relative orientation of the magnetic field \mathbf{B} with respect to the density structures, showing that: (1) The magnetic field shows a preferential orientation parallel to most of the density structures in the three simulations. (2) The orientation of \mathbf{B} changes from parallel to perpendicular to the density structures in regions with density over a critical density n_T in the highest magnetization case. (3) The change of relative orientation with respect to density is largest for the highest magnetization and decreases in lower magnetization cases. This effect is also present in the projected maps, where we consider the relative orientation of column density structures and polarization pseudovectors. The described change in the relative orientation of the magnetic field is potentially measurable using submillimeter polarization observations of molecular clouds and can be used to complement the estimates of magnetic field strength found with techniques based on the Chandrasekhar-Fermi method. In conjunction with simulations HROs can be used to establish a link between the observed morphology in polarization maps and the physics of molecular clouds.

Subject headings: ISM: magnetic fields, ISM: clouds, polarization, submillimeter

1. INTRODUCTION

The study of the magnetic field in molecular clouds is crucial to understand the physical processes relevant in molecular cloud evolution and star formation (Shu et al. 1987; McKee & Ostriker 2007; Crutcher 2012). A long-standing technique used to infer the morphology of the magnetic field projected on the plane of the sky is the measurement of polarization of visible and near-infrared light background stars (Hiltner 1949; Davis & Greenstein 1951; Heiles & Haverkorn 2012). This technique assumes that aspherical dust grains are aligned with respect to the interstellar magnetic field and the observed position angle of linear polarization is parallel to the plane-of-the-sky projection of the field (Davis & Greenstein 1951).

A more recent complementary technique is the measurement of the thermal polarized emission of dust in the submillimeter wavelengths (Hildebrand et al. 1984; Novak et al. 1997; Vaillancourt 2007). Measurable de-

grees of polarization on the order of a few percent are typical for interstellar clouds in the submillimeter and the far-infrared (Benoît et al. 2004; Vaillancourt 2011). The mechanism which produces the alignment of the grains is still the subject of active research (Lazarian & Hoang 2007). However, there is firm evidence indicating that it results from radiative torques produced by anisotropic radiation flux with respect to the magnetic field (Hoang & Lazarian 2008). Theoretical understanding of the grain alignment indicates that even in relatively dense clouds (visual extinction $A_V \sim 10$), dust polarization traces the underlying magnetic field (Bethell et al. 2007).

The strength of the magnetic field has been estimated from observations of the projected component on the plane of the sky using the Chandrasekhar-Fermi method (Chandrasekhar & Fermi 1953; Houde et al. 2009; Novak et al. 2009) and comparing the observed morphology with theoretical models (Koch et al. 2012). In parallel, significant efforts have been made to relate the magnetic field morphology inferred from polarization to the observed structure in both observed (Li et al. 2009; Chapman et al. 2011) and simulated clouds (Ostriker et al. 2001; Nakamura & Li 2008). In the case of pre-stellar cores, a number of observations reveal an hourglass morphology in the magnetic field (Girart et al. 2006; Attard et al. 2009), and in the case of larger structures, the morphological analysis relies on visual inspection and statistics of the orientation angles (Goldsmith et al. 2008). The results of observations

¹ Department of Astronomy & Astrophysics, University of Toronto, Toronto, ON Canada M5S 3H4; soler@astro.utoronto.ca

² Laboratoire de Radioastronomie, École Normale Supérieure and Observatoire de Paris, UMR CNRS 8112. 24 rue Lhomond 75231 Paris Cedex 05, France

³ Canadian Institute for Theoretical Astrophysics, University of Toronto, 60 St. George Street, Toronto, ON M5S 3H8, Canada

⁴ Institut d'Astrophysique Spatiale CNRS, Université Paris-Sud, bâtiment 121, 91405, Orsay, France

⁵ Department of Physics, University of Toronto, 60 St. George Street, Toronto, ON M5S 1A7, Canada

are inconclusive in establishing a global trend of relative alignment between the magnetic field and the structure (Goodman et al. 1990). However, theory and simulations establish very clear scenarios in which the relative orientation of the field reveals the role of magnetism in the formation of structures the cloud (Fiege & Pudritz 2000; Nakamura & Li 2008).

Recent observations by the ESA Herschel Mission reveal ubiquitous filamentary structures in molecular clouds (Peretto et al. 2012; André et al. 2010; Molinari et al. 2010). These observations together with starlight polarization measurements have been used to investigate the physical conditions of gravitational collapse and star formation within the filaments. Seminal examples in which the inferred magnetic field direction in adjacent lower density material is perpendicular to the densest filaments are in Taurus (Chapman et al. 2011; Palmeirim et al. 2013), Serpens (Sugitani et al. 2011), and the Pipe Nebula (Alves et al. 2008). These studies provide insight into the physical processes involved in the formation of filamentary structure but they do not probe the complex relationship of column density and magnetic field morphologies in the dense regions of molecular clouds, where stars predominantly form and which are fundamental to establishing a global picture of molecular cloud formation (Lada et al. 2010).

The advent of new instruments for measuring the thermal dust polarized emission such as ALMA (Peck & Beasley 2008), BLASTPol (Pascale et al. 2012) and *Planck* (Planck Collaboration et al. 2011) which measure polarization in scales ranging from pre-stellar cores to entire molecular cloud complexes, motivates a common scheme for the morphological analysis of polarization maps. It is in this context that we introduce the Histogram of Relative Orientation (HRO), a statistical tool for characterizing column density morphologies on multiple scales. This technique, developed for pattern recognition in machine vision, uses the gradient to characterize the directionality of the density structure in a 2D map and here in a 3D simulated cube. It provides a robust characterization of the density field that can be used with polarization observations to investigate the relative orientation of density structure with respect to the magnetic field.

This paper is organized as follows: Section 2 introduces the method of Histogram of Relative Orientation and implementation details of the technique are described in Appendix A. Section 3 introduces the simulated molecular clouds used to characterize our statistical tool and details are given in Appendix B. Section 4 presents the HRO analysis of 3D simulated clouds and Section 5 shows how the proposed diagnostic obtained in 3D can also be found in the projected 2D maps. Finally Section 6 summarizes the results and discusses the application of HROs to observations of real molecular clouds.

2. THE HISTOGRAM OF RELATIVE ORIENTATIONS

The Histogram of Relative Orientation (HRO) is inspired by a family of detection algorithms usually called Histograms of Oriented Gradients (HOGs, Leonardis et al. 2006). HOGs are used in pattern recognition and are developed in the context of machine vision. These algorithms use the gradient to describe the orien-

tation of the edges in an image. The gradient is based on the difference between pixels in a neighborhood and quantifies the edges: the magnitude carries the information on the difference (edge strength) and the orientation defines the direction perpendicular to a contour line (edge direction). A histogram of the orientation angles of the gradient rotated by 90° therefore summarizes statistically the orientation of the features in an image. Further refinement of this method includes weighting the contribution of each pixel (or voxel in 3D) to the histogram by the magnitude of the gradient at each point, allowing characterization of the image using only the stronger edges.

In HROs, the computation of the gradient is performed using Gaussian derivative kernels. The size of the Gaussian determines the area of the vicinity over which the gradient will be calculated. Varying the size of the Gaussian kernel enables the sampling of different scales and reduces the effect of noise in the pixels.

The HROs use the gradient of the density in 3D simulated cubes to generate a vector field which characterizes isodensity contours and can be directly compared to the magnetic field vectors. In 2D, the gradient of the column density ($\nabla\Sigma$) is compared to the orientation of the linear polarization field, which is a pseudovector since it is invariant to a $\pm 180^\circ$ rotation.

The implementation of the HROs is discussed in detail in Appendix A.

3. MODEL PARAMETERS

The cloud models used to characterize HRO are the result of magneto-hydrodynamical simulations produced with the RAMSES-MHD code (Teyssier 2002; Fromang et al. 2006). These clouds are isothermal with $T = 11.44$ K (sound speed $c_s = 0.2$ km s $^{-1}$) for regions with density less than 10^4 times the initial density n_0 and adiabatic for larger densities. The solutions are obtained in a cubic box of side L with initial uniform density $n_0 = n_{H_2} = 536.41$ cm $^{-3}$, which is comparable to the density in the Taurus-Auriga Dark Cloud Complex (Stahler & Palla 2005). The boundary conditions of the box are periodic.

The relative importance of gravity and thermal pressure forces is related to L and n_0 . For this analysis we have chosen $L = 4$ pc; the Jeans length $L_J \equiv c_s(\pi/G\rho_0)^{1/2}$ is 0.88 pc for $\rho_0 = \mu n_0$ and $\mu = 2.4 m_p$. The total mass in the simulated cubes is $2.04 \times 10^3 M_\odot$ and with $L = 4$ pc, it is comparable to small regions within Dark Cloud Complexes such as Lupus I (Cambr sy 1999).

Turbulence in the simulation is introduced as an initial isotropic random velocity field $\delta\mathbf{v}$ with a Kolmogorov spectrum (see Appendix B). This velocity field is not driven and decays during the cloud evolution. All simulations are initiated with kinetic energy $E_K = 100\bar{\rho}L^3c_s^2$ corresponding to an initial Mach number $\mathcal{M} \equiv \sigma_v/c_s = 10$ and include gravity.

Three different initial magnetization cases are considered and parameterized by the ratio of the isothermal sound speed to the initial Alfv n speed or equivalently, the ratio of the plasma pressure to the initial magnetic pressure: $\beta \equiv c_s^2/v_{A,0}^2 = \bar{\rho}c_s^2/(B_0^2/4\pi)$. We consider a “quasi-hydrodynamical” model with $\beta = 100.0$, an “in-

TABLE 1
MODEL PARAMETERS AND TIMES OF
SNAPSHOTS

β	$\langle B_0 \rangle$ (μG)	Snapshot Age (Myr)	(t_g^a)	(t_f^b)
100.0	0.35	0.48	0.11	0.25
100.0	0.35	1.16	0.27	0.60
1.0	3.47	0.69	0.16	0.36
1.0	3.47	1.32	0.31	0.68
0.1	10.97	0.61	0.14	0.32
0.1	10.97	1.15	0.27	0.59

^a Characteristic gravitational time scale $t_g = 4.27$ Myr

^b Flow crossing time scale $t_f = 1.95$ Myr

intermediate magnetization” model with $\beta = 1.0$, and a “high magnetization” model with $\beta = 0.1$. The physical value of the magnetic field is given by:

$$B_0 = \beta^{-1/2} \mu\text{G} \left(\frac{T}{10 \text{ K}} \right)^{1/2} \left(\frac{n_{H_2}}{100 \text{ cm}^{-3}} \right)^{1/2} \quad (1)$$

For the chosen initial density and temperature, the corresponding uniform magnetic field strengths are 0.35, 3.47, and 10.97 μG . The evolved fields are spatially nonuniform and can differ greatly from the initial values although the volume-averaged magnetic field is a constant $B_0 \hat{x}$ in time. The value of β is proportional to the the mass-to-magnetic flux ratio in the simulation and cannot change with time.

The initial Alfvén Mach number $\mathcal{M}_A \equiv \langle v^2/v_A^2 \rangle^{1/2} = \mathcal{M}\beta^{1/2}$ is 100, 10, and 3.16 for $\beta = 100.0$, 1.0, and 0.1 respectively, and therefore all models considered have initially supersonic and super-Alfvénic flow. The initially uniform clouds are unstable to compressions transverse to the mean magnetic field (“magneto-Jeans unstable”) when the magneto-sonic wave crossing time exceeds the characteristic gravitational contraction time, t_g (Chandrasekhar & Fermi 1953). All models would be unstable by the magneto-Jeans criterion ($L/L_J = 4.56 < \beta^{-1/2}$). The three simulations are initially supercritical, with the mass M to magnetic flux Φ_g ratio under the critical value ($M/\Phi_g)_{crit} = 1/(2\pi G^{1/2})$, and $(M/\Phi_g)/(M/\Phi_g)_{crit} \approx t_g v_A/(\pi L)$ is equal to 0.01, 0.07, and 0.22.

In Table 1, we describe the simulation snapshots under consideration in terms of the sound crossing time $t_v \equiv L/c_s = 19.5$ Myr, which is fixed owing to the *isothermal* equation of state, the flow crossing time $t_f \equiv L/\sigma_v = 1.95$ Myr, where we use the Mach number associated with the initial turbulent velocity and the characteristic gravitational time scale, $t_g \equiv (\pi/G\bar{\rho})^{1/2} = 4.27$ Myr. Two snapshots in this study are taken: one at $t_1 \sim 0.03 t_v$ and another at $t_2 \sim 0.06 t_v$. As in preceding studies (Ostriker et al. 2001; Heitsch et al. 2001), this paper concentrates on structures that form as a consequence of turbulence, before gravity becomes important. The snapshots are taken at $t_1 < t_2 < t_g$ when shock fronts moving through the gas initiate the formation of filaments and knots.

Further details of the numerical methods used in the simulations are given in Appendix B.

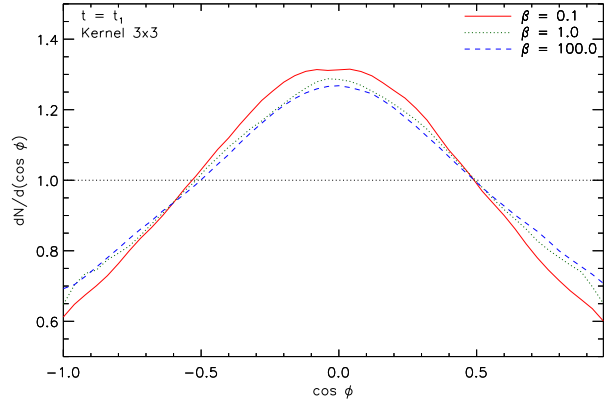


FIG. 1.— Histogram of Relative Orientation showing the cosine of the angle between the magnetic field vector \mathbf{B} and the gradient of the density ∇n for the low, intermediate, and high-magnetization simulation cubes ($\beta = 100$, 1.0, and 0.1) in a snapshot taken at $t \sim 0.06 t_v$. The histogram is normalized such that a random distribution of \mathbf{B} and ∇n would equal unity in each bin (black dotted line). The histograms calculated from the simulated cubes show a peak at $\cos \phi \sim 0$ which corresponds to the magnetic fields predominantly tracing the isodensity contours.

4. HRO APPLIED TO SIMULATION CUBES

The simulated cube contains the density, velocity, and magnetic field values for every voxel. The HROs are used to summarize the relative orientation of the magnetic field vector \mathbf{B} with respect to the gradient of the density ∇n in each one of these voxels following the procedure described in Section 2. The histogram of the angle ϕ between two sets of random vectors in 3D is not uniform, i.e., in 3D, two random vectors are more likely to be perpendicular than parallel. In 3D the uniformly distributed quantity is $\cos \phi$ and therefore we choose that quantity for the histogram.

4.1. Results of the HROs 3D Analysis

Figure 1 shows the HRO corresponding to all of the voxels in each of the three simulations for a snapshot at $t_2 \sim 0.3 t_g$. The peak at $\cos \phi = 0$ shows that ∇n is predominantly oriented perpendicular to \mathbf{B} in the three simulations. This corresponds to \mathbf{B} mostly parallel to the isodensity contours in the simulated volume.

The two snapshots considered here correspond to $t < t_g$ and $t < t_v$. At these time scales, the dynamics of the gas are dominated by shocks and the over-densities are not formed by self-gravitation. The relative orientation revealed by the HRO is the result of the magnetic field becoming strongly bent and stretched. The imprint of the initial magnetization was found by studying and comparing the relative orientation in the highest densities regions. In these regions, the relative orientation is the consequence of the locally strong self-gravity and the interaction of the gas and the magnetic field.

The colored curves in Figure 2 correspond to the HRO of regions in a particular density bin. The red and magenta curves correspond to regions with the highest densities, the gray and blue curves to regions with densities close to the mean density of the cube ($\log \bar{n} = 2.73$) and all others to intermediate densities. The algorithm used to segment the cube in these density bins is described in Section A.3.

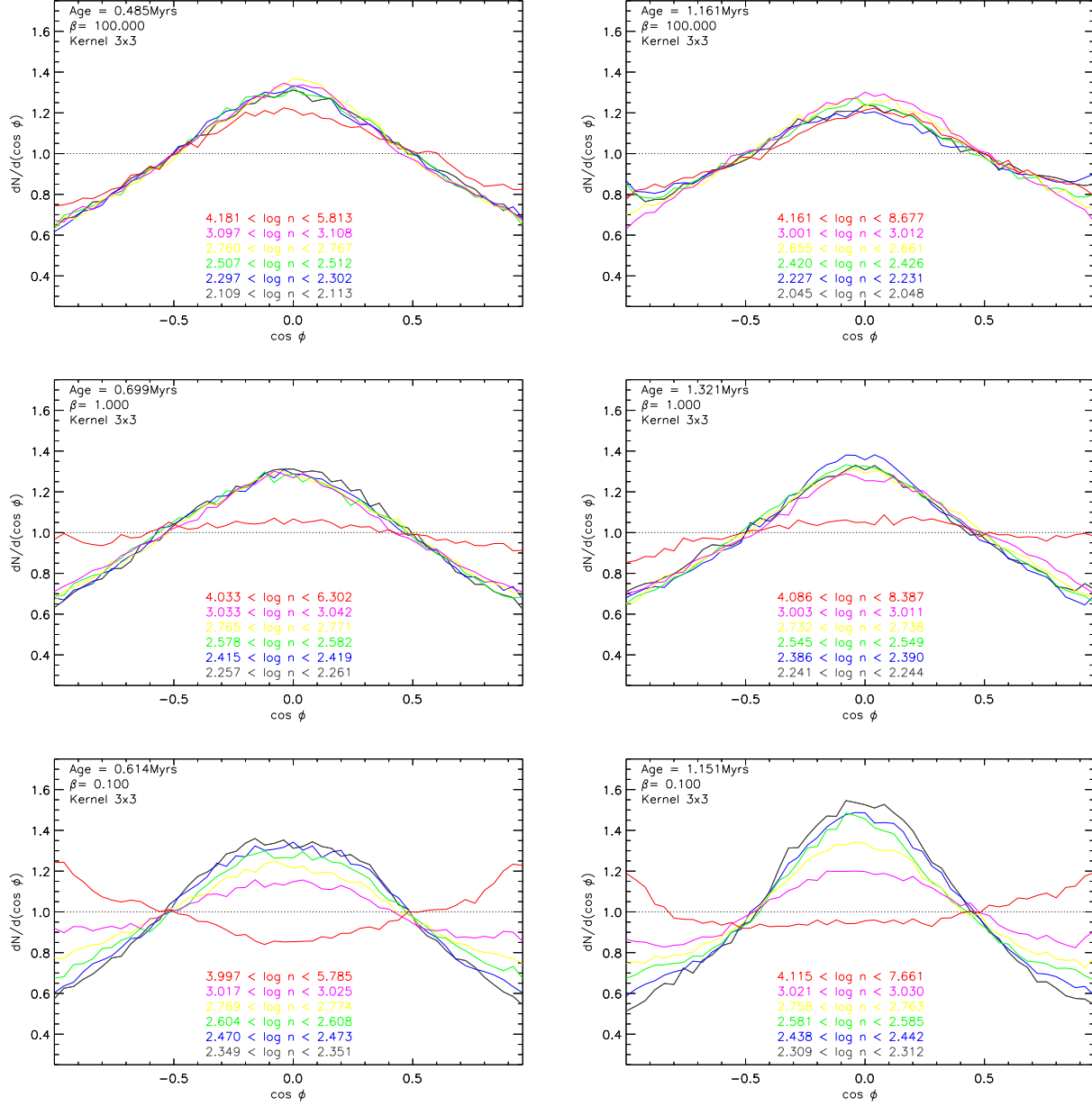


FIG. 2.— HROs corresponding to simulated cubes with $\beta=100.0$ (top), 1.0 (middle), and 0.1 (bottom) in snapshots taken at $t \sim 0.03 t_v$ (left) and $t \sim 0.06 t_v$ (right). The colored curves within each plot correspond to voxels in the density ranges indicated in the figure. The histograms in the low magnetization case (top) peak at $\cos \phi \sim 0$ in regions with densities $n \geq \bar{n}$ which corresponds to the magnetic field (\mathbf{B}) predominantly tracing the isodensity contours even at the greatest densities. The histograms from the intermediate (middle) and high magnetization (bottom) cases also peak at $\cos \phi \sim 0$ in regions with densities $n \sim \bar{n}$. However, the histograms flatten in higher density regions. At the highest densities the histograms peak at $\cos \phi \sim \pm 1$. This corresponds to \mathbf{B} tracing the isodensity contours in regions with $n \sim \bar{n}$, then showing no particular relative orientation in intermediate density regions, and being oriented perpendicular to the isodensity contours in the highest density regions.

Figure 2 illustrates the difference in the relative orientation of ∇n and \mathbf{B} in low and high density regions in simulations with low and high magnetization. In the low and intermediate magnetization cases ($\beta = 100$ and $\beta = 1$), ∇n and \mathbf{B} are preferentially perpendicular to each other, which corresponds to \mathbf{B} parallel to the isodensity contours. In the case of greater magnetization ($\beta = 0.1$), ∇n is mostly perpendicular to \mathbf{B} at densities close to the mean but the relative orientation progressively changes when considering regions with greater densities until ∇n and \mathbf{B} are predominantly parallel to

each other.

With this progressive change in relative orientation, the HRO curve changes from convex to concave. To quantify this behavior we define the histogram shape parameter:

$$\zeta \equiv A_c - A_e \quad (2)$$

A_c is the area under the central region of the HRO curve ($-0.25 < \cos \phi < 0.25$) and A_e is the area in the

extremes of the HRO curve ($-1.00 < \cos \phi < -0.75$ and $0.75 < \cos \phi < 1.00$). This parameter characterizes a curve peaking at $\cos \phi \sim 0.0$ (convex) as $\zeta > 0.0$ whereas a curve peaking at $\cos \phi \sim \pm 1.0$ (concave) corresponds to $\zeta < 0.0$ and a flat distribution corresponds to $\zeta \sim 0$. The uncertainty in the determination of ζ is related to the standard deviation around the calculated area in each region, i.e.,

$$\sigma_\zeta \equiv \sqrt{\sigma_{A_c}^2 + \sigma_{A_e}^2} \quad (3)$$

With these definitions, a noisy HRO will either produce $\zeta \sim 0$ which is consistent with a random relative orientation or will increase σ_ζ to a level in which it describes no preferential orientation.

Figure 3 shows the value of ζ for the different column density segments in all six simulations. The red curve illustrates the progressive change of the relative orientation of ∇n and \mathbf{B} with density in the simulations with the greatest magnetization: it changes from \mathbf{B} preferentially parallel to the isodensity contours ($\zeta > 0$) for densities close to the mean ($\log n [\text{cm}^{-3}] \sim 2.7$) to \mathbf{B} perpendicular to the isodensity contours ($\zeta < 0$) in the regions with densities higher than about $6\bar{n}$. The curves corresponding to low and intermediate magnetization also show a similar change in the relative orientation of ∇n and \mathbf{B} with density although it is less pronounced. Thus we find that the slope of ζ as a function of the mean density in the density bin is a parameter which characterizes the initial magnetization state of the simulated cloud.

Additionally, we find that ζ becomes negative (\mathbf{B} is preferentially perpendicular to the isodensity contours) at the highest densities in the highest magnetization case. The value of the threshold density, n_T , above which ∇n and \mathbf{B} are predominantly parallel (ζ becomes negative) is also a parameter which characterizes the magnetization state of the simulated cloud: higher magnetization corresponds to lower values of n_T .

4.2. Discussion

We have found two features of the relative orientation of ∇n and \mathbf{B} which characterize the initial magnetization: 1. The rate of change from perpendicular ∇n and \mathbf{B} to parallel in regions with increasing mean bin density. 2. The value of the density n_T over which ∇n and \mathbf{B} are parallel. We observe that the rate of change of ζ is greater and that n_T is lower with higher magnetization. These effects are related to the balance between the magnetic forces, the turbulence and the gravitational forces in each simulation.

The three simulations are initially supercritical. Supercritical clouds can collapse both parallel and perpendicular to the field with unlimited asymptotic density, as opposed to subcritical clouds which can collapse along the field but not perpendicular to it, forming flattened structures where the peak density would be limited by the thermal pressure.

The supersonic perturbations resulting from the initial turbulence are amplified or suppressed depending on the strength of the initial magnetic field (Draine & McKee 1993). The dynamical importance of the magnetic field before self-gravity becomes important can be estimated by comparing the initial magnetic energy density $B^2/8\pi$

and the initial kinetic energy density $\rho\sigma_v^2/2$. This ratio is $(v_A/\sigma_v)^2 = 1/(\mathcal{M}^2\beta)$ and it is equal to 0.001, 0.1, and 1.0 for the low, intermediate, and high magnetization. In the low magnetization case, the Alfvén speed $v_A < c_s$ and the kinetic energy density is dominant. In consequence, the fields become strongly bent by motions of the matter. In the high magnetization case, the magnetic and the kinetic energy are closer initially, and with $v_A > c_s$, the matter is constrained to move along stiff magnetic field lines.

The relative orientation between supersonic shock fronts and the magnetic field could in principle be the mechanism which produces over-densities with a particular orientation with respect to \mathbf{B} . Alignment between \mathbf{B} and the gas velocity field has been reported in previous works (Banerjee et al. 2009); however the exact process which causes this relative orientation is not well understood yet. The relative orientation of \mathbf{B} perpendicular to the over-densities is close to the scenario described by Mouschovias (1976). However, the interaction between supersonic turbulence and magnetic field which produces the final configuration of \mathbf{B} and density structures is still the subject of active research (Klessen 2011; Schneider et al. 2011; Hennebelle & Falgarone 2012).

In the low-magnetization case, ∇n is perpendicular to \mathbf{B} (\mathbf{B} along isodensity contours) even in the regions with the highest densities. In this case, the gravitational forces dominate over the magnetic field ($(M/\Phi_g)/(M/\Phi_g)_{crit} \approx 0.01$) and in the densest regions the decrease of ζ is related to the isotropic gravitational collapse breaking the alignment of ∇n perpendicular to \mathbf{B} , leading to $\zeta \sim 0$ in the densest regions.

In the high-magnetization cases, ∇n is parallel to \mathbf{B} (\mathbf{B} perpendicular to the isodensity contours) in the regions with the highest densities. In this case, the gravitational forces are less dominant ($(M/\Phi_g)/(M/\Phi_g)_{crit} \approx 0.22$) and the channeling of the flow along the magnetic field is reinforced by the perpendicular magnetic support against gravitational collapse, leading to flattened structures perpendicular to the magnetic field which correspond to $\zeta < 0$ in the densest regions.

5. HRO APPLIED TO OBSERVATIONS OF THE SIMULATION CUBES

The HRO analysis is applied to the maps of the column density Σ and polarization obtained by integrating the six simulated data cubes along three different lines of sight (x, y, or z-axis). Details of the model of projection using Equation B1 are given in Appendix B.1. The projection of the Stokes parameters into the plane of the sky incorporates a grain alignment efficiency model described in Equation B2. This uses the density in each voxel as a proxy for what might actually be a column density dependence of the grain alignment mechanism. Here we compare results for uniform alignment efficiency ($\epsilon = 1$) with the results for a model with $\epsilon = 1$ at $n < n_0$ but decreasing ϵ with increasing n in regions with $n > n_0$.

The grain alignment is locally such that the polarization vector is perpendicular to the magnetic field. The projected polarization is therefore perpendicular to a weighted projection of the magnetic field, a pseudovector that we call \mathbf{B}_{POS} .

The HROs of the simulated maps are calculated using a process analogous to that used in the 3D data cubes.

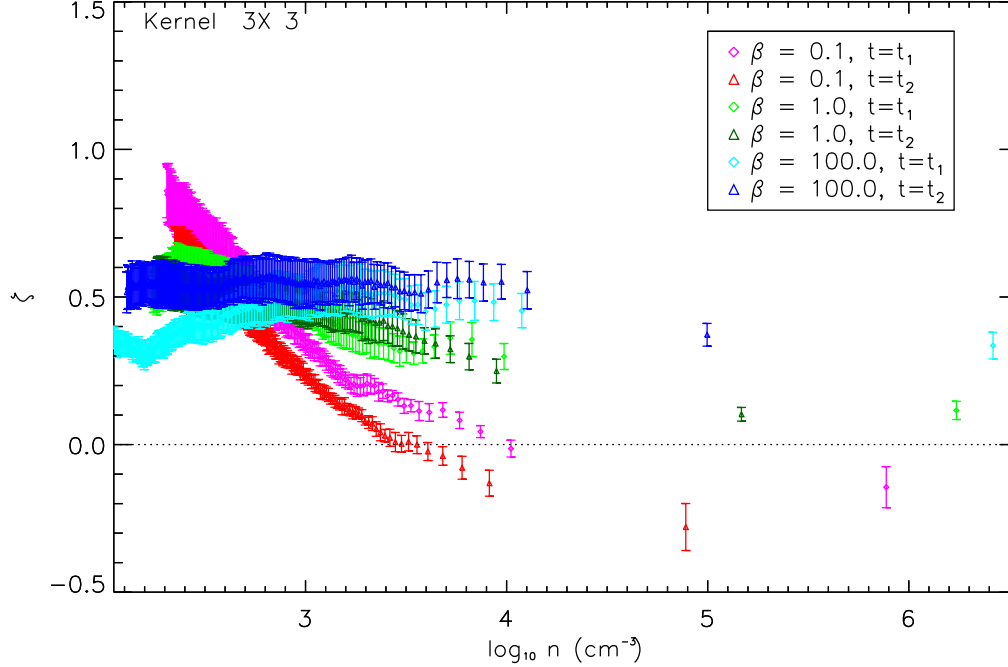


FIG. 3.— HRO shape parameter ζ which parameterizes the relative orientation of the magnetic field (\mathbf{B}) and the gradient of the density ∇n . $\zeta > 0.0$ corresponds to a HRO showing \mathbf{B} predominantly perpendicular to ∇n (\mathbf{B} parallel to the isodensity contours). $\zeta \sim 0.0$ corresponds to a flat HRO showing no predominant relative orientation between \mathbf{B} and ∇n . $\zeta < 0.0$ corresponds to a HRO showing \mathbf{B} predominantly parallel to ∇n (\mathbf{B} perpendicular to the isodensity contours). The HROs of the low magnetization case show \mathbf{B} predominantly parallel to the isodensity contours with $\zeta > 0.0$ even in the higher density regions. In contrast, the HROs of the high magnetization cases show \mathbf{B} parallel to the isodensity contours with $\zeta > 0.0$ in the low density regions, changing to \mathbf{B} perpendicular to the isodensity contours, with $\zeta < 0.0$ in the highest density regions. The shape parameter ζ as a function of density decreases faster in higher magnetization simulations.

The histogram of the angle ϕ between two sets of random vectors in 2D is uniform, and therefore we choose ϕ as the variable.

5.1. Results of the HROs 2D Analysis

Figure 4 shows the HROs corresponding to the angle ϕ between the projected magnetic field pseudovector \mathbf{B}_{POS} and the gradient of the column density $\nabla \Sigma$ in the projected maps. The peak at 90° reveals that the relative orientation between ∇n and \mathbf{B} observed in the 3D (Figure 1) is also present in the polarization and column density maps and \mathbf{B}_{POS} predominantly follows the iso- Σ contours. This result can be confirmed by visual inspection of the \mathbf{B}_{POS} and Σ maps as shown in Figure 5.

As in Section 4, we divided the maps in column density bins to check how the relative orientation changes in the highest density regions. Figure 6 shows the HRO curves corresponding to different column density regimes. The behavior of the HROs in 2D is very similar to that observed in the 3D analysis: \mathbf{B}_{POS} and $\nabla \Sigma$ are mainly perpendicular in all the Σ bins of the low-magnetization map. The HROs of the intermediate and high-magnetization cases show \mathbf{B}_{POS} and $\nabla \Sigma$ predominantly perpendicular in regions of the map with $\Sigma \sim \bar{\Sigma}$ and parallel in the regions of the map with the greatest Σ .

In the same way as in the 3D analysis, the change in the HRO curves is parameterized by the histogram shape parameter ζ defined in Equation 4.1. In this case

A_C is the area under the central region of the HRO curve ($67.5^\circ < \phi < 112.5^\circ$) and A_e is the area in the extremes of the HRO curve ($0^\circ < \phi < 22.5^\circ$ and $157.5^\circ < \phi < 180^\circ$). Figure 7 shows the value of ζ as a function of the central column density of each bin. The HROs of the low magnetization case show \mathbf{B}_{POS} predominantly parallel to the isodensity contours with $\zeta > 0.0$ even in the highest Σ regions. In contrast, the HROs of the intermediate and high magnetization cases show \mathbf{B}_{POS} parallel to the isodensity contours with $\zeta > 0.0$ but changing into \mathbf{B}_{POS} perpendicular to the isodensity contours with $\zeta < 0.0$ predominately in the highest Σ regions.

5.2. Discussion

There are two main effects to be considered in the recovery of the imprint of magnetization on the relative orientation in the projected maps. First is the effect of the integration along the line of sight. The second is the effect of the alignment efficiency in weighting the reconstruction of the projected magnetic field.

Figure 7 shows that the relative orientation in the projected map is analogous to the one measured in 3D: \mathbf{B}_{POS} and $\nabla \Sigma$ are preferentially aligned perpendicular to each other. In 3D the highest density regions where we observed \mathbf{B} perpendicular to the isodensity contours are surrounded by lower density shells where \mathbf{B} is parallel to the isodensity. In 2D we observed \mathbf{B}_{POS} parallel to $\nabla \Sigma$ in the highest density regions of the map showing that the relative orientation in the lower density shell

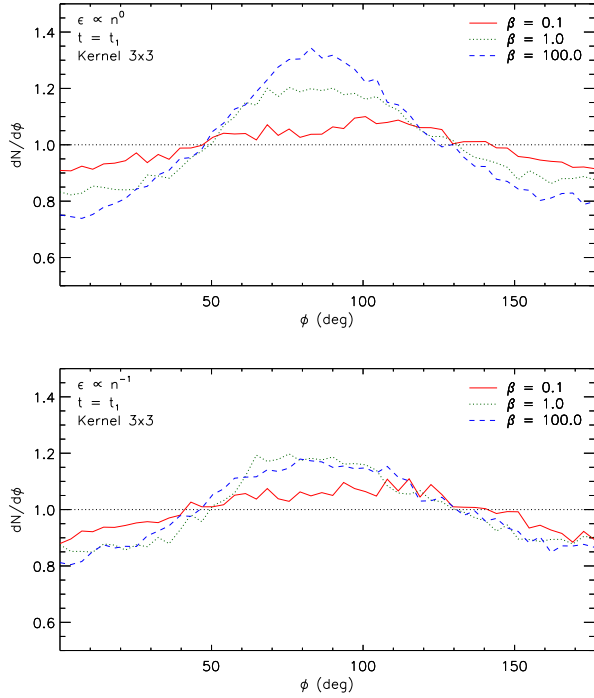


FIG. 4.— Histogram of Relative Orientation showing the angle between the projected magnetic field pseudovector \mathbf{B}_{POS} and the gradient of the column density $\nabla\Sigma$ in projections of the low, intermediate, and high-magnetization simulation cubes ($\beta = 100, 1.0$, and 0.1) in a snapshot taken at $t \sim 0.06 t_v$ and using grain alignment efficiency from Equation B2 with $p = 0$ (top) and $p = -1$ (bottom). The projections are obtained following Equation B1. The histogram is normalized such that a random distribution of \mathbf{B}_{POS} and $\nabla\Sigma$ would equal unity in each bin (black dotted line). The histograms calculated from the simulated cubes show a peak at $\phi \sim 90^\circ$ which corresponds to the magnetic fields predominantly tracing iso- Σ contours.

does not dominate in the projected map. More detailed modeling of the integration along the line of sight and its effect on the HROs and ζ will be the subject of future studies.

An interesting issue for the line of sight integration is the relative orientation of the mean magnetic field with respect to the line of sight. All of the results presented here correspond to lines of sight perpendicular to the plane of the initial magnetic field (Y or Z for initial \mathbf{B} along the X axis). Small variations about this orientation of the mean magnetic field with respect to the line of sight do not affect the conclusions of the HRO study. However, the HROs corresponding to projections along the X-axis (line of sight parallel to the initial magnetic field direction) are not distinctively different for different initial magnetization. Thus, further studies are required to draw conclusions from observations of clouds where the mean magnetic field is oriented very close to the line of sight.

The effect of the alignment efficiency is illustrated in the two plots in Figure 7. The slopes of the $\zeta - \Sigma$ curves corresponding to different initial magnetization are clearly distinguishable in the case of uniform $\epsilon = 1$. However, when considering a decreasing alignment efficiency, $\epsilon \propto n^{-1}$, the curves corresponding to the low and intermediate magnetization are degenerate and only

the curve corresponding to the highest magnetization is distinctive.

We find that the slope of the $\zeta - \Sigma$ curve is strongly dependent on the grain alignment mechanism, which is yet to be understood. In spite of that, $\zeta < 0$ corresponds to magnetic field dominance. The column density Σ_T at which the relative orientation changes can be used potentially to estimate the magnitude of \mathbf{B}_{POS} .

6. SUMMARY AND DISCUSSION

We have introduced the Histogram of Relative Orientations (HRO), a tool to study the relative orientation of the magnetic field and the structure in MHD simulations and in polarization observations. The HRO quantifies the relative orientation of the magnetic field \mathbf{B} and the isodensity contours. The contours are characterized by the gradient of the density ∇n in the simulated volume or the gradient of the column density $\nabla\Sigma$ in projections of the simulations.

Using HROs on a set of simulated molecular clouds with decaying supersonic turbulence and with low, intermediate, and high initial magnetization ($\beta = 100.0, 1.0$, and 0.1) we found a significant imprint of the magnetization in the relative orientation of the magnetic field and the density structures. We found that \mathbf{B} is oriented predominantly parallel to the isodensity contours in the three simulations. However, on dividing the simulated region into density bins and considering the relative orientation in each bin, in the high magnetization simulation we found that at the highest densities \mathbf{B} becomes perpendicular to the isodensity contours.

We parameterize the change in relative orientation with the histogram shape parameter ζ . We show the behavior of ζ in regions with different densities in the simulated volume (Figure 3) and different column densities in the projected map (Figure 7). The study of this change in relative orientation can be applied to observations of molecular clouds. Establishing a link between observations and MHD simulations will provide an opportunity to study the role of the magnetic field in the formation of structures in molecular clouds.

HROs can also be applied to observations where the polarization pseudovectors are only available on sparse regions of the map. Additionally HROs can use a range of gradient kernels to sample a particular range of scales and reduce the effect of the noise in the observed maps. With the aid of further simulations, the column density Σ_T at which the field changes its relative orientation may be used to estimate the strength of the magnetic field in the plane of the sky, complementing current estimates obtained with the Chandrasekhar-Fermi method.

6.1. Relation to Existing Studies

Studies of the morphology of the polarization observations and its relation to the magnetic field strength in molecular clouds have generally been based on the Chandrasekhar-Fermi method (Chandrasekhar & Fermi 1953; Houde et al. 2009). These studies relate the dispersion of the polarization orientation to the magnetic field strength in the cloud, an effect which is evident in the previous studies of MHD simulations (Ostriker et al. 2001, 1999) and in the polarization maps obtained from the simulation set in this paper (Figure 5).

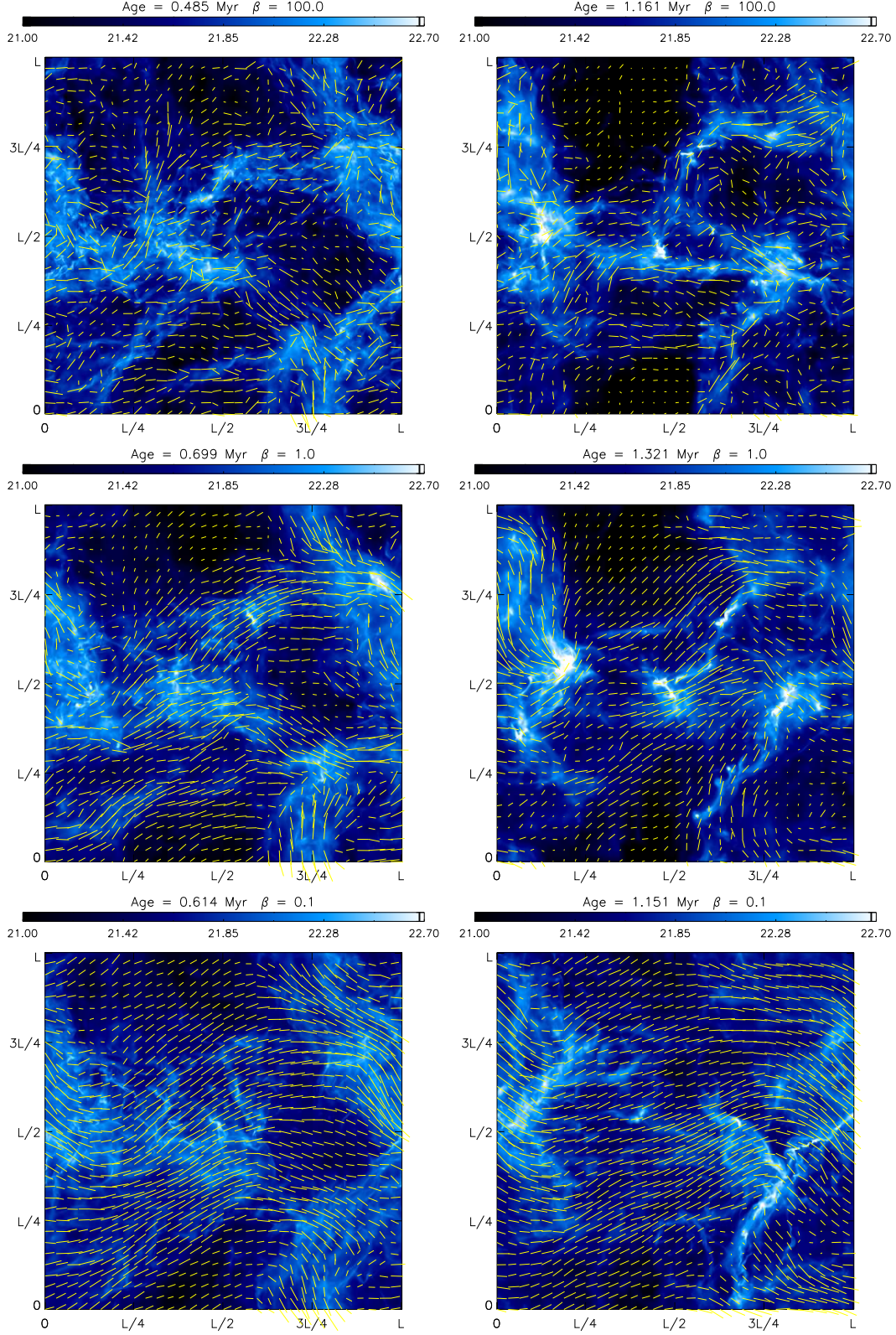
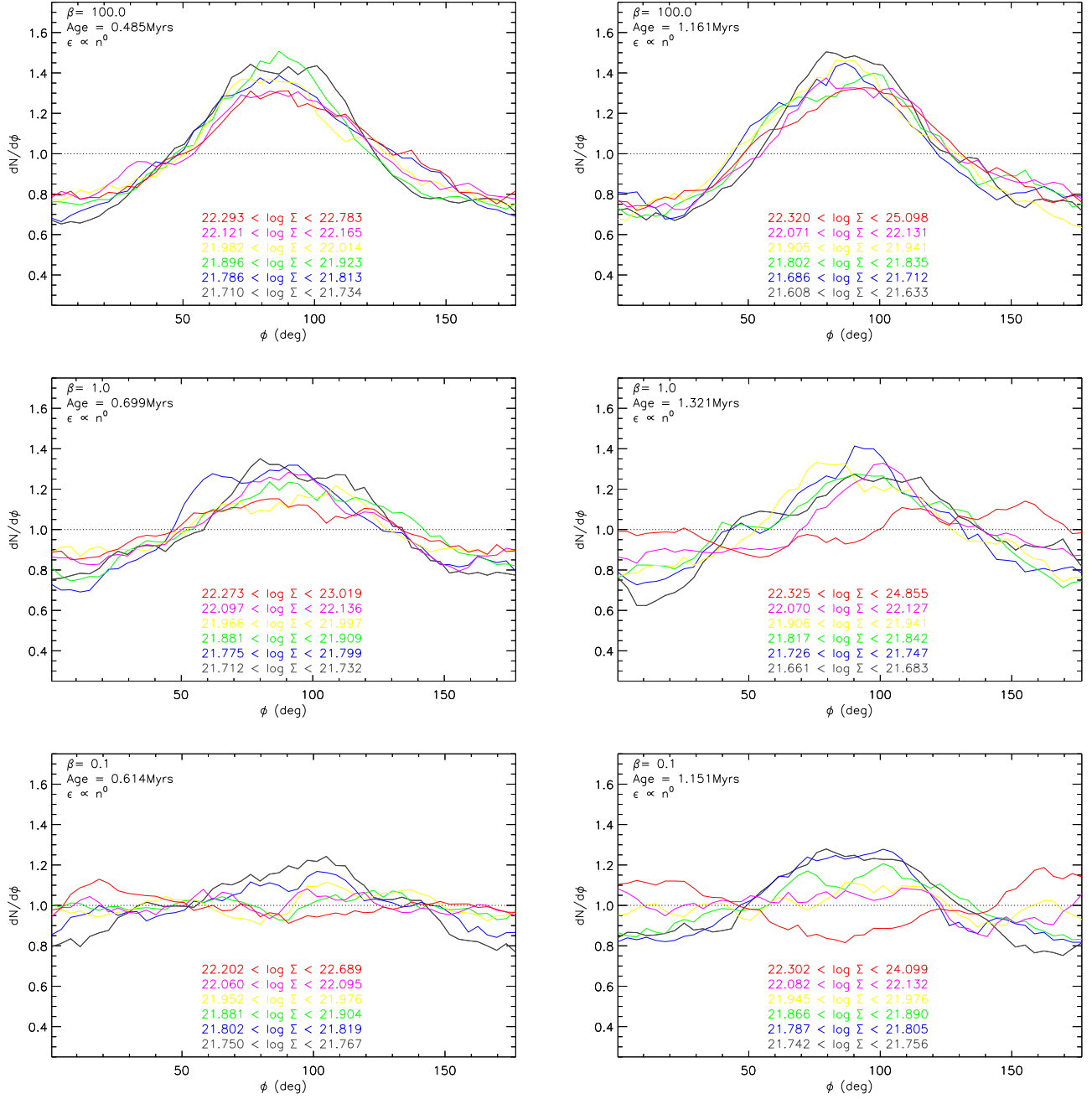


FIG. 5.— Maps of the logarithm of the column density ($\log \Sigma$) and overlaid magnetic field pseudovectors as determined by Equations B1 and B2 with $p = -1$ and $n_0 = 500 \text{ cm}^{-3}$. These maps correspond to projections along the z-axis of simulations with $\beta = 100$ (top), 1.0 (middle), and 0.1 (bottom) in snapshots taken at $t \sim 0.03 t_v$ (left) and $t \sim 0.06 t_v$ (right).



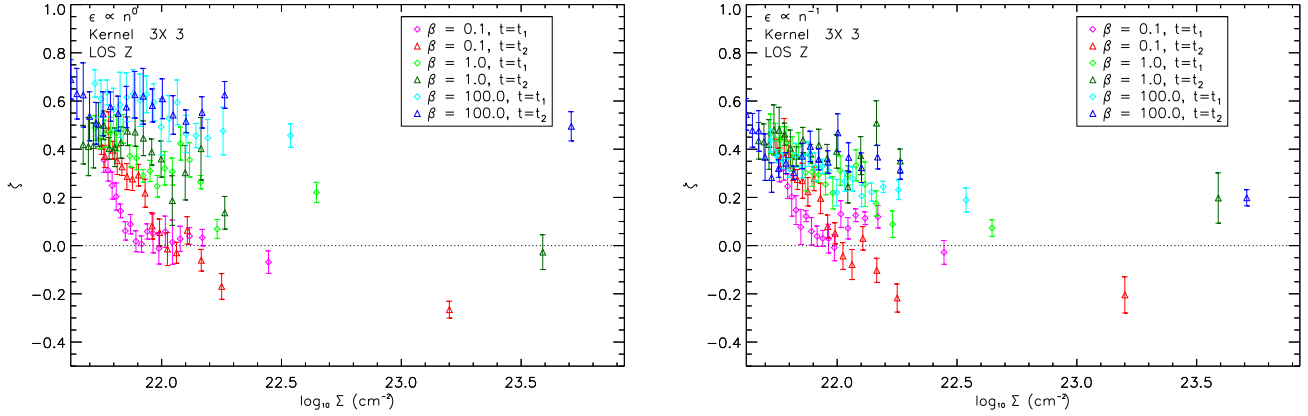


FIG. 7.— Histogram of Relative Orientation shape parameter ζ which parameterizes the relative orientation of the projected magnetic field (\mathbf{B}_{POS}) and the gradient of the column density $\nabla\Sigma$. $\zeta > 0.0$ corresponds to a HRO showing \mathbf{B}_{POS} predominantly perpendicular to $\nabla\Sigma$ (\mathbf{B}_{POS} parallel to the iso- Σ contours). $\zeta \sim 0.0$ corresponds to a flat HRO showing no predominant relative orientation between \mathbf{B}_{POS} and $\nabla\Sigma$. $\zeta < 0.0$ corresponds to a HRO showing \mathbf{B}_{POS} predominantly parallel to $\nabla\Sigma$ (\mathbf{B}_{POS} perpendicular to the iso- Σ contours). As in the 3D case, the HROs of the low magnetization case show \mathbf{B}_{POS} predominantly parallel to the isodensity contours with $\zeta > 0.0$ even in the higher density regions. In contrast, the HROs of the intermediate and high magnetization cases show \mathbf{B}_{POS} parallel to the isodensity contours with $\zeta > 0.0$ at low densities and changing into \mathbf{B}_{POS} perpendicular to the isodensity contours, with $\zeta < 0.0$ in the highest density regions. The shape parameter ζ as a function of density decreases faster for the higher magnetization simulations.

An alternative approach is the study of the relative orientation of the magnetic field inferred from polarization observations and the orientation of the column density structure. In a seminal work Goodman et al. (1990) considered the alignment of starlight polarization and extinction maps in six different molecular clouds and found no particular orientation which globally described the observations. Similar studies (Tassis et al. 2009; Sugitani et al. 2011; Palmeirim et al. 2013) have considered a qualitative description to relate the magnetic field observations to the formation of the filamentary structure. HROs represent a quantitative tool to evaluate the relative orientation of the magnetic field and create a general scheme to compare observations of different clouds with the results of MHD simulations.

The observed morphology of the submillimeter polarized emission from the dense regions in molecular clouds (Vaillancourt & Matthews 2012) shows a diversity of relative orientations which can potentially be correlated with the magnetic field in each region. Koch et al. (2012) have already found a correlation between the iso- Σ contours and the inferred magnetic field directions which is used to fit a model of the magnetic field. The HRO provides a common scheme to relate these observations to larger scale observations which cover entire cloud complexes.

6.2. HROs and Future Work

In this article we have focused our studies to the case of an isothermal molecular cloud with a particular behavior of turbulence and magnetization in order to characterize our method. Nevertheless, the HRO analysis can be extended to simulations including more complex realizations of molecular clouds (Nakamura & Li 2008; Hennebelle et al. 2008). Characterization using HROs allow us to link a large volume of polarization observations with the great diversity of physics which can be modeled in MHD simulations.

The HROs of the simulations discussed in this paper

evaluate the relative orientation in scales ranging from 2.34×10^{-2} pc to 3.83×10^{-1} pc (kernels of 3×3 to 49×49 pixels), which correspond to angular scales of $\sim 10''$ to $\sim 10'$ for a cloud located at a distance of 150 pc.

The results of the HRO analysis show that the imprint of magnetization on the molecular cloud is present in at least two diagnostics of the relative orientation of the magnetic field:

1. The change in the relative orientation of \mathbf{B} and the column density structures as a function of column density.
2. The value of the column density Σ_T at which B shifts from parallel to perpendicular to the iso- Σ contours.

These two parameters allow the systematic comparison of simulations and observations; however, characterization of the magnetization conditions using these diagnostics should be accompanied by careful modeling of the grain alignment efficiency.

The study of multiple ages, environments and dominant physics in simulations is one of the primary challenges facing the construction of a complete and coherent picture of the star formation process. The advent of results from experiments such as *Planck* (Planck Collaboration et al. 2011), ALMA (Peck & Beasley 2008), PILOT (Bernard et al. 2010), BLASTPol (Pascale et al. 2012), and SOFIA (Vaillancourt et al. 2007) will produce an unprecedented volume of observations of molecular clouds. In the future, the use of HROs and complementary tools will facilitate the systematic characterization of synthetic observations, and identify the common elements in the observations and models that reveal the role of the magnetic field and turbulence in the formation of structure in the interstellar medium.

We gratefully acknowledge G. Novak and T. Matthews

for the helpful comments on the manuscript. We are indebted to F. Flores-Mangas for providing useful insight into machine vision algorithms and to C. Matzner for his comments on the physics of shocks. This work was supported in part by the Natural Sciences and Engineering Research Council of Canada

(NSERC), the Canadian Space Agency (CSA) and the Canadian Institute for Advance Research (CIFAR). Computations were performed at Sunnyvale, the beowulf cluster at the Canadian Institute for Theoretical Astrophysics. The simulations are part of the StarFormat database and are publicly available at <http://starformat.obspm.fr/starformat/projects>.

APPENDIX CONSTRUCTION OF THE HRO

The implementation of the HROs is made with the procedure described in the following subsections.

Calculation of the Gradient

The orientation of the isodensity contours are characterized by the gradient of density:

$$\nabla n = \left(\frac{\partial n}{\partial x} \right)_l \hat{x} + \left(\frac{\partial n}{\partial y} \right)_l \hat{y} + \left(\frac{\partial n}{\partial z} \right)_l \hat{z} \quad (\text{A1})$$

The subindex l is related to the size of the area on which the gradient is calculated or as subsequently shown, the size of the Gaussian derivative kernel. To zeroth order, the components of the gradient can be calculated using forward differences of adjacent pixels:

$$\frac{\partial n}{\partial x} \sim n(x+1, y) - n(x, y) \quad (\text{A2})$$

Derivatives are linear and shift-invariant, and so the gradient calculation can be done using convolution. Forward differences can be calculated using the 2×2 Roberts kernels, but such a small kernel is too sensitive to noise. The calculation of the gradient can be improved by using the central difference:

$$\frac{\partial n}{\partial x} = \frac{n(x+1, y) - n(x-1, y)}{2}, \quad \frac{\partial n}{\partial y} = \frac{n(x, y+1) - n(x, y-1)}{2} \quad (\text{A3})$$

The corresponding kernels for convolution calculation are the 3×3 Prewitt kernels:

$$\frac{\partial}{\partial x} = \frac{1}{6} \begin{pmatrix} -1 & 0 & 1 \\ -1 & 0 & 1 \\ -1 & 0 & 1 \end{pmatrix}, \quad \frac{\partial}{\partial y} = \frac{1}{6} \begin{pmatrix} -1 & -1 & -1 \\ 0 & 0 & 0 \\ 1 & 1 & 1 \end{pmatrix} \quad (\text{A4})$$

Noise reduction can be achieved by averaging over the vicinity of each pixel. For the convolution method this is implemented to first order using the 3×3 Sobel kernels. Convoluting with these kernels is equivalent to smoothing the image over a 3×3 region and then calculating first derivatives, which is a particular case of the Gaussian Derivatives method:

$$\frac{\partial}{\partial x} = \begin{pmatrix} -1 & 0 & 1 \\ -2 & 0 & 2 \\ -1 & 0 & 1 \end{pmatrix}, \quad \frac{\partial}{\partial y} = \begin{pmatrix} -1 & -2 & -1 \\ 0 & 0 & 0 \\ 1 & 2 & 1 \end{pmatrix} \quad (\text{A5})$$

Gaussian Derivatives

Convolution and differentiation are commutative and associative; therefore the smoothing and derivative operators can be written as:

$$\frac{\partial}{\partial x}(I \star G) = I \star \frac{\partial}{\partial x}G \quad (\text{A6})$$

G is the 2D-Gaussian kernel and I is a 2D image. This equation implies that filtering an image and subsequently calculating the gradient is equivalent to the convolution of the image with a kernel that is the first derivative of a gaussian kernel. This operation is called a Gaussian derivative (Young 1986).

For the present study, we use the Gaussian derivatives method and following Equation A6 we obtained each component of the gradient in Equation A.1 by convoluting slices of the density cube $N_k \equiv n_{ijk}$ and $N_i \equiv n_{ijk}$ with a kernel formed by the derivative of a $l \times l$ two-dimensional Gaussian G :

$$\begin{aligned} \left(\frac{\partial n}{\partial x} \right)_l &= N_k \star \frac{\partial}{\partial x}G \\ \left(\frac{\partial n}{\partial y} \right)_l &= N_k \star \frac{\partial}{\partial y}G \\ \left(\frac{\partial n}{\partial z} \right)_l &= N_i \star \frac{\partial}{\partial x}G \end{aligned} \quad (\text{A7})$$

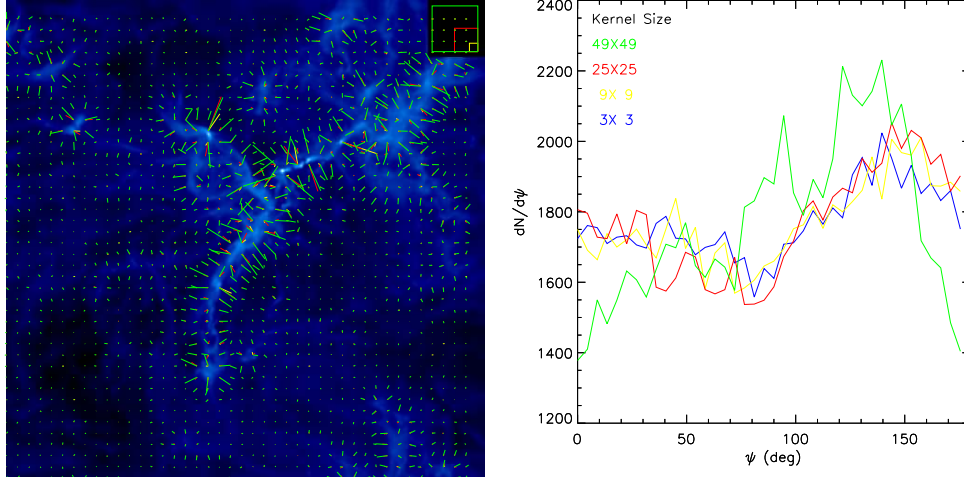


FIG. 8.— Left: Filamentary structure in the simulated column density. Overlaid are the gradient vectors obtained with derivative kernels with 9×9 (yellow), 25×25 (red), and 49×49 (green) pixels. The squares on the upper right corner of the image show the sizes of these kernels. Right: Histogram of orientation angles of the iso- Σ contours (ψ) calculated with each derivative kernel. The histograms show that the structure is predominantly oriented at ψ from 135° to 150° but also shows a secondary structure at 45° (ψ is measured counterclockwise from the top of the map, using the convention for position angles of polarization).

and in the 2D projected maps

$$\begin{aligned} \left(\frac{\partial \Sigma}{\partial x} \right)_l &= \Sigma \star \frac{\partial}{\partial x} G \\ \left(\frac{\partial \Sigma}{\partial y} \right)_l &= \Sigma \star \frac{\partial}{\partial y} G \end{aligned} \quad (\text{A8})$$

Figure 8 illustrates the characterization of a simulated image using the gradient of the column density $\nabla \Sigma$. The vectors plotted over the image show the direction of the gradient obtained using Gaussian kernels of different sizes. The histogram shows the orientation angles of the structures in the image, measured counterclockwise with respect to the y-axis of the image (convention for polarization position angles). Each peak in the histogram corresponds to a dominant orientation of the features in the image. A histogram of a completely random map would be flat. The histogram of a straight rod would be a delta function centered on its orientation angle. The histogram of a blob would have a peak corresponding to the orientation of its semi-major axis.

Calculation of the Angle

The angle ϕ between the gradient and the magnetic field at each voxel is calculated using a combination of the scalar and vector product of vectors:

$$\phi = \arctan \left(\frac{\mathbf{B} \times \nabla n}{\mathbf{B} \cdot \nabla n} \right) \quad (\text{A9})$$

The result of this calculation is a cube (a map in 2D) with values of ϕ at each voxel (pixel in 2D). As explained in Section 4, in the study of the alignment in 3D it is more natural to construct the HROs as a function of $\cos \phi$ and not directly ϕ . The angle between the isodensity contours and the magnetic field is $\phi \pm 90^\circ$. The histogram of values of $\cos \phi$ (ϕ in 2D) weighted by the magnitude of the gradient at each voxel (pixel) is what we call Histogram of Relative Orientations.

Figure 9 shows a histogram of $\cos \phi$ calculated on a simulated cube and ϕ calculated on a projection of the cube using three derivative kernels. Using these three kernels we observe the same preferential relative orientation between \mathbf{B} and ∇n in the cube and \mathbf{B}_{POS} and $\nabla \Sigma$ in the projection.

Segmentation

Individual regions of an image can be studied by dividing the images into bins of the parameters that define it and subsequently masking each bin. This process is known in computer science as image segmentation. Segmentation is a subject of active research in computer science and its implementation in 3D (2D) HROs is limited to dividing the cube (image) in density (column density) bins with equal number of voxels (pixels).

The objective of the segmentation is the study and comparison of the relative orientation in density regimes where the dominant physical processes and the dust alignment efficiency ϵ are different. The segmentation by column density of the maps resulting from the projection of the simulated cubes is illustrated in the left-hand side of Figure 10. Using the column density distribution, which is close to log-normal, we produce density bins with equal number of pixels. An equal number of gradient vectors in each bin guarantees comparable statistics for each density bin.

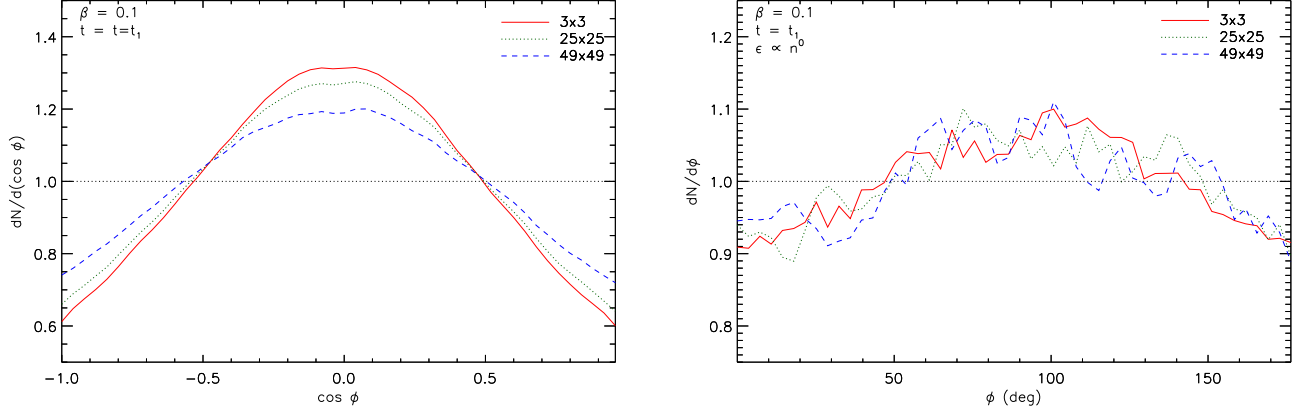


FIG. 9.— HROs obtained by applying three different derivative kernels to the $\beta = 0.1$ simulation cube (left) and to a projected map obtained by integrating the cube along the z-axis (right). The similarity of the curves within each plot shows that the predominant relative orientation is present in regions with scales ranging from 3 pixels to 49 voxels (pixels).

The segmentation by density or column density is motivated by the change of physical conditions in the densest regions with respect to less dense regions. In the densest regions self-gravity becomes relevant and the kinetic energy density is lower than the magnetic energy density, in contrast with the less dense regions where the balance between magnetic and turbulent energy is different. The segmentation of maps by polarization percentage, line of sight velocity or polarization angle dispersion is a potentially useful way to study physical processes in observations of molecular clouds and will be addressed in future works.

MOLECULAR CLOUD SIMULATIONS

The model clouds are created by integrating the compressible ideal MHD equations using the RAMSES-MHD code (Teyssier 2002; Fromang et al. 2006). RAMSES-MHD is a N-body and MDH code with 3D Adaptive Mesh Refinement (AMR). The refinement criteria are based on density as described in Dib et al. (2010). RAMSES-MHD uses constrained transport to guarantee that $\nabla \cdot \mathbf{B} = 0$ to machine accuracy at all time and uses the MUSCL-Hancock scheme, a finite volume method that combines good accuracy with fast execution. The solutions are obtained in a cubic box of side L with grids of 512^3 zones, integrated from the AMR cubes with effective resolution 2048^3 . We apply periodic boundary conditions in all models, simulating a portion of the interior of a molecular cloud.

The energy equation used in this simulation set is the barotropic equation of state: for densities under the critical density parameter ($n_c = 5.364 \times 10^7 \text{ cm}^{-3}$) the gas is isothermal with sound speed $c_s = 0.2 \text{ km s}^{-1}$, which corresponds to a temperature of 11.44 K. In the absence of fully time-dependent radiative transfer this represents a reasonable first approximation for the gas at volume densities higher than the mean (comprising most of the matter) for conditions appropriate to molecular clouds (Scalo et al. 1998). When the density reaches n_c , the gas becomes adiabatic.

The gravitational potential is computed from the density using standard Fourier methods. The periodic boundary conditions exclude the $\mathbf{k} = 0$ component of the density. Therefore, the gravitational potential ϕ_G obeys the modified Poisson equation $\nabla^2 \phi_G = 4\pi G(\rho - \bar{\rho})$, where $\bar{\rho} = M/L^3$ is the mean density (mass divided by the volume of the box).

Turbulence in the simulation is introduced as a random velocity field $\delta \mathbf{v}$. $\delta \mathbf{v}$ is a Gaussian random perturbation field with a power spectrum $|\delta v_{\mathbf{k}}|^2 \propto k^{-11/3}$, subject to the constraint $\nabla \cdot \delta \mathbf{v} = 0$ so that the initial velocity is non-compressive. This spectrum corresponds to the Kolmogorov energy spectrum, $E(k) \propto k^{-5/3}$, and it is comparable to the spectrum inferred for large-scale cold interstellar clouds (Larson 1981) and the spectrum that naturally follows from the evolution of incompressible turbulence. An identical realization of the initial velocity field is used for all of the models, so that the initial states of the simulations differ only in the strength of the mean magnetic field. The turbulence decays during the cloud evolution (it is not driven).

Projecting 3D Data Cubes with Magnetic Field to 2D Maps with Polarization

The observed intensity of the polarized emission results from the combined effect of the dust grain alignment efficiency ϵ and integration along the line of sight. The radiative torques mechanism (Lazarian & Hoang 2007) indicates that the degree of alignment depends on the exposure of the grains to an anisotropic starlight background. This dependence implies that the radiative torques mechanism should be more efficient in regions of relatively low extinction.

The maps of the Stokes parameters I, Q, and U are produced by integrating the density n and the magnetic field \mathbf{B}

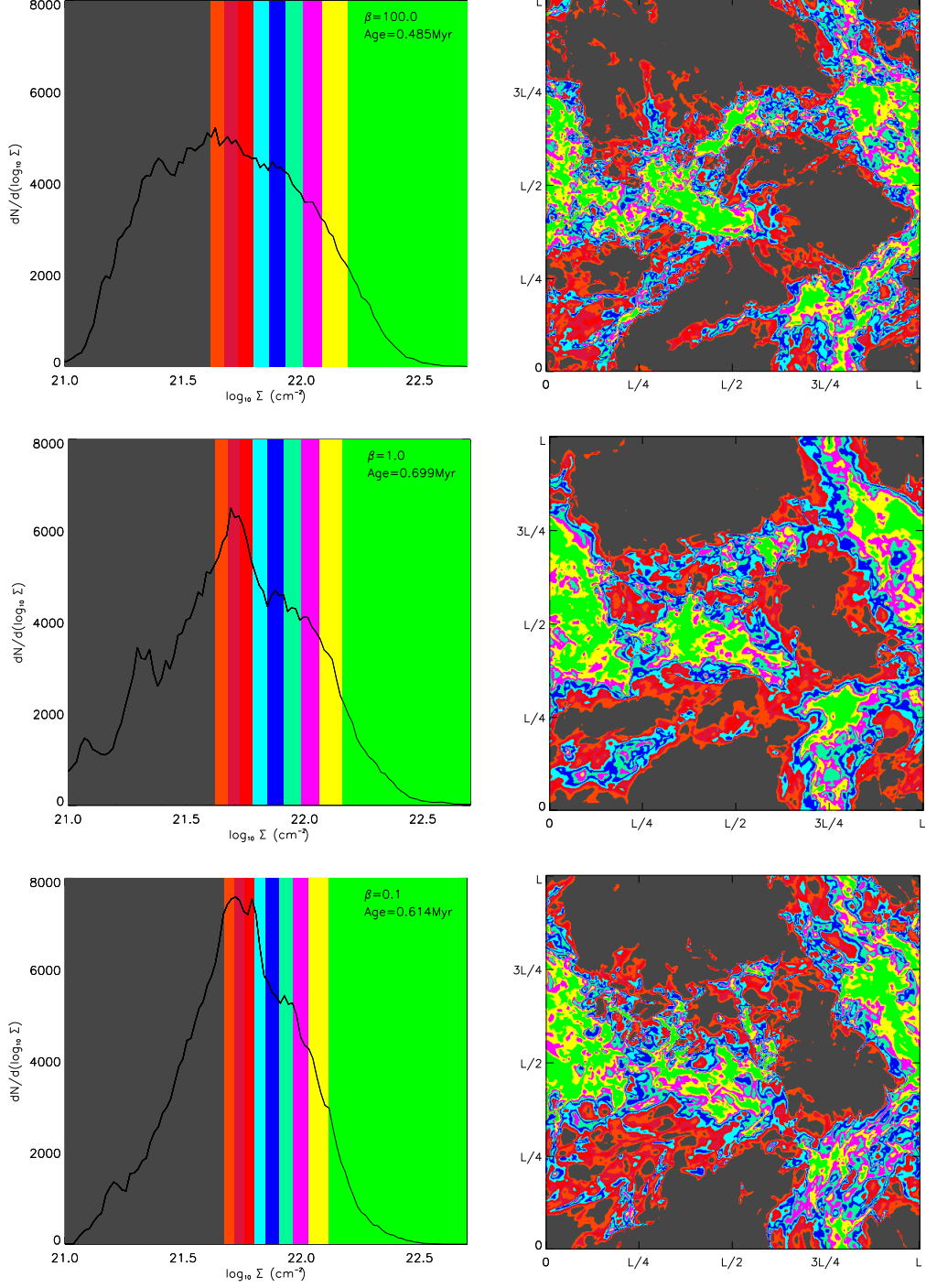


FIG. 10.— Example of the map segmentation process introduced in Section A.3. Left: Column density distribution in projections of three simulations. Overlaid colors correspond to density bins with equal number of pixels used in HRO analysis. Right: Column density maps of the projections of three simulations. Overlaid colors correspond to regions with column densities shown in the histograms.

in the cube along the k -direction (either x , y or z) according to:

$$\begin{aligned}
 I_{ij} &\propto \Sigma_{ij} = \sum_k n_{ijk} \\
 Q_{ij} &\propto \sum_k \epsilon_{ijk} n_{ijk} (B_{ijk}^{(i)} B_{ijk}^{(i)} - B_{ijk}^{(j)} B_{ijk}^{(j)}) \\
 U_{ij} &\propto \sum_k 2\epsilon_{ijk} n_{ijk} B_{ijk}^{(i)} B_{ijk}^{(j)}
 \end{aligned} \tag{B1}$$

In this study we use the density as a proxy of the column density dependence of ϵ . For each cell of the simulated data cube we evaluate:

$$\epsilon_{ijk} = \begin{cases} (n_{ijk})^p & \text{if } n_{ijk} \geq n_0 \\ 1.0 & \text{if } n_{ijk} < n_0 \end{cases} \quad (\text{B2})$$

In this toy-model, $p < 0$ accounts for depolarization effects (Matthews et al. 2001; Houde et al. 2002) in high column density regions. $p = 0$ is used to test the line of sight integration independently of the environment dependence of ϵ . In this study we have chosen $n_0 = 500 \text{ cm}^3$, corresponding to a relatively diffuse region within a molecular cloud. We present results obtained with $p = 0$ and $p = -1$. These choices intend to reproduce some of the effects observed in polarization maps. A more detailed calculation of ϵ , including modeling the grain alignment mechanisms is beyond the scope of this work.

The polarization percentage P is calculated as:

$$P_{ij} = \frac{\sqrt{Q_{ij}^2 + U_{ij}^2}}{I_{ij}} \quad (\text{B3})$$

This quantity, of particular observational interest (Matthews & Wilson 2002; Martin 2007), is shown for reference in Figure 11 as a function of column density Σ in projections of three simulations for two models of ϵ , with $p = 0$ and $p = -1$. The different distributions seen there and the systematic behavior, specially the decline of P with increasing Σ in the right panels, offer diagnostics relating parameters in MHD simulations to observations.

REFERENCES

- Alves, J., Lombardi, M., & Lada, C. J. 2008, *The Pipe Nebula: A Young Molecular Cloud Complex*, ed. B. Reipurth, 415
- André, P., Men'shchikov, A., Bontemps, S., et al. 2010, *A&A*, 518, L102
- Attard, M., Houde, M., Novak, G., et al. 2009, *ApJ*, 702, 1584
- Banerjee, R., Vázquez-Semadeni, E., Hennebelle, P., & Klessen, R. S. 2009, *MNRAS*, 398, 1082
- Benoît, A., Ade, P., Amblard, A., et al. 2004, *A&A*, 424, 571
- Bernard, J.-P., Ade, P., Andre, Y., et al. 2010, in *COSPAR Meeting*, Vol. 38, 38th COSPAR Scientific Assembly, 4075
- Bethell, T. J., Chepurnov, A., Lazarian, A., & Kim, J. 2007, *ApJ*, 663, 1055
- Cambrésy, L. 1999, *A&A*, 345, 965
- Chandrasekhar, S., & Fermi, E. 1953, *ApJ*, 118, 113
- Chapman, N. L., Goldsmith, P. F., Pineda, J. L., et al. 2011, *ApJ*, 741, 21
- Crutcher, R. M. 2012, *ARA&A*, 50, 29
- Davis, Jr., L., & Greenstein, J. L. 1951, *ApJ*, 114, 206
- Dib, S., Hennebelle, P., Pineda, J. E., et al. 2010, *ApJ*, 723, 425
- Draine, B. T., & McKee, C. F. 1993, *ARA&A*, 31, 373
- Fiege, J. D., & Pudritz, R. E. 2000, *ApJ*, 544, 830
- Fromang, S., Hennebelle, P., & Teyssier, R. 2006, *A&A*, 457, 371
- Girart, J. M., Rao, R., & Marrone, D. P. 2006, *Science*, 313, 812
- Goldsmith, P. F., Heyer, M., Narayanan, G., et al. 2008, *ApJ*, 680, 428
- Goodman, A. A., Bastien, P., Menard, F., & Myers, P. C. 1990, *ApJ*, 359, 363
- Heiles, C., & Haverkorn, M. 2012, *Space Sci. Rev.*, 166, 293
- Heitsch, F., Zweibel, E. G., Mac Low, M.-M., Li, P., & Norman, M. L. 2001, *ApJ*, 561, 800
- Hennebelle, P., Banerjee, R., Vázquez-Semadeni, E., Klessen, R. S., & Audit, E. 2008, *A&A*, 486, L43
- Hennebelle, P., & Falgarone, E. 2012, *A&A Rev.*, 20, 55
- Hildebrand, R. H., Dragovan, M., & Novak, G. 1984, *ApJ*, 284, L51
- Hiltner, W. A. 1949, *Science*, 109, 165
- Hoang, T., & Lazarian, A. 2008, *MNRAS*, 388, 117
- Houde, M., Vaillancourt, J. E., Hildebrand, R. H., Chitsazadeh, S., & Kirby, L. 2009, *ApJ*, 706, 1504
- Houde, M., Bastien, P., Dotson, J. L., et al. 2002, *ApJ*, 569, 803
- Klessen, R. S. 2011, in *EAS Publications Series*, Vol. 51, *EAS Publications Series*, ed. C. Charbonnel & T. Montmerle, 133–167
- Koch, P. M., Tang, Y.-W., & Ho, P. T. P. 2012, *ApJ*, 747, 79
- Lada, C. J., Lombardi, M., & Alves, J. F. 2010, *ApJ*, 724, 687
- Larson, R. B. 1981, *MNRAS*, 194, 809
- Lazarian, A., & Hoang, T. 2007, *MNRAS*, 378, 910
- Leonardis, A., Bischof, H., & Pinz, A., eds. 2006, *Lecture Notes in Computer Science*, Vol. 3951, *Histograms of Oriented Gradients for Human Detection*, ed. A. Leonardis, H. Bischof, & A. Pinz (Springer)
- Li, H.-b., Dowell, C. D., Goodman, A., Hildebrand, R., & Novak, G. 2009, *ApJ*, 704, 891
- Martin, P. G. 2007, in *EAS Publications Series*, Vol. 23, *EAS Publications Series*, ed. M.-A. Miville-Deschênes & F. Boulanger, 165–188
- Matthews, B. C., & Wilson, C. D. 2002, *ApJ*, 571, 356
- Matthews, B. C., Wilson, C. D., & Fiege, J. D. 2001, *ApJ*, 562, 400
- McKee, C. F., & Ostriker, E. C. 2007, *ARA&A*, 45, 565
- Molinari, S., Swinyard, B., Bally, J., et al. 2010, *A&A*, 518, L100
- Mouschovias, T. C. 1976, *ApJ*, 206, 753
- Nakamura, F., & Li, Z.-Y. 2008, *ApJ*, 687, 354
- Novak, G., Dotson, J. L., Dowell, C. D., et al. 1997, *ApJ*, 487, 320
- Novak, G., Dotson, J. L., & Li, H. 2009, *ApJ*, 695, 1362
- Ostriker, E. C., Gammie, C. F., & Stone, J. M. 1999, *ApJ*, 513, 259
- Ostriker, E. C., Stone, J. M., & Gammie, C. F. 2001, *ApJ*, 546, 980
- Palmeirim, P., André, P., Kirk, J., et al. 2013, *A&A*, 550, A38
- Pascale, E., Ade, P. A. R., Angile, F. E., et al. 2012, in *Society of Photo-Optical Instrumentation Engineers (SPIE) Conference Series*, Vol. 8444, *Society of Photo-Optical Instrumentation Engineers (SPIE) Conference Series*
- Peck, A. B., & Beasley, A. J. 2008, *Journal of Physics Conference Series*, 131, 012049
- Peretto, N., André, P., Könyves, V., et al. 2012, *A&A*, 541, A63
- Planck Collaboration, Ade, P. A. R., Aghanim, N., et al. 2011, *A&A*, 536, A1
- Scalo, J., Vázquez-Semadeni, E., Chappell, D., & Passot, T. 1998, *ApJ*, 504, 835
- Schneider, N., Bontemps, S., Simon, R., et al. 2011, *A&A*, 529, A1
- Shu, F. H., Adams, F. C., & Lizano, S. 1987, *ARA&A*, 25, 23
- Stahler, S. W., & Palla, F. 2005, *The Formation of Stars*
- Sugitani, K., Nakamura, F., Watanabe, M., et al. 2011, *ApJ*, 734, 63
- Tassis, K., Dowell, C. D., Hildebrand, R. H., Kirby, L., & Vaillancourt, J. E. 2009, *MNRAS*, 399, 1681
- Teyssier, R. 2002, *A&A*, 385, 337
- Vaillancourt, J. E. 2007, in *EAS Publications Series*, Vol. 23, *EAS Publications Series*, ed. M.-A. Miville-Deschênes & F. Boulanger, 147–164
- Vaillancourt, J. E. 2011, in *Astronomical Society of the Pacific Conference Series*, Vol. 449, *Astronomical Society of the Pacific Conference Series*, ed. P. Bastien, N. Manset, D. P. Clemens, & N. St-Louis, 169
- Vaillancourt, J. E., & Matthews, B. C. 2012, *ApJS*, 201, 13
- Vaillancourt, J. E., Chuss, D. T., Crutcher, R. M., et al. 2007, in *Society of Photo-Optical Instrumentation Engineers (SPIE) Conference Series*, Vol. 6678, *Society of Photo-Optical Instrumentation Engineers (SPIE) Conference Series*
- Young, R. A. 1986, *Simulation of Human Retinal Function with the Gaussian Derivative Model*. General Motors Corporation Research Laboratories. Computer Science Dept.

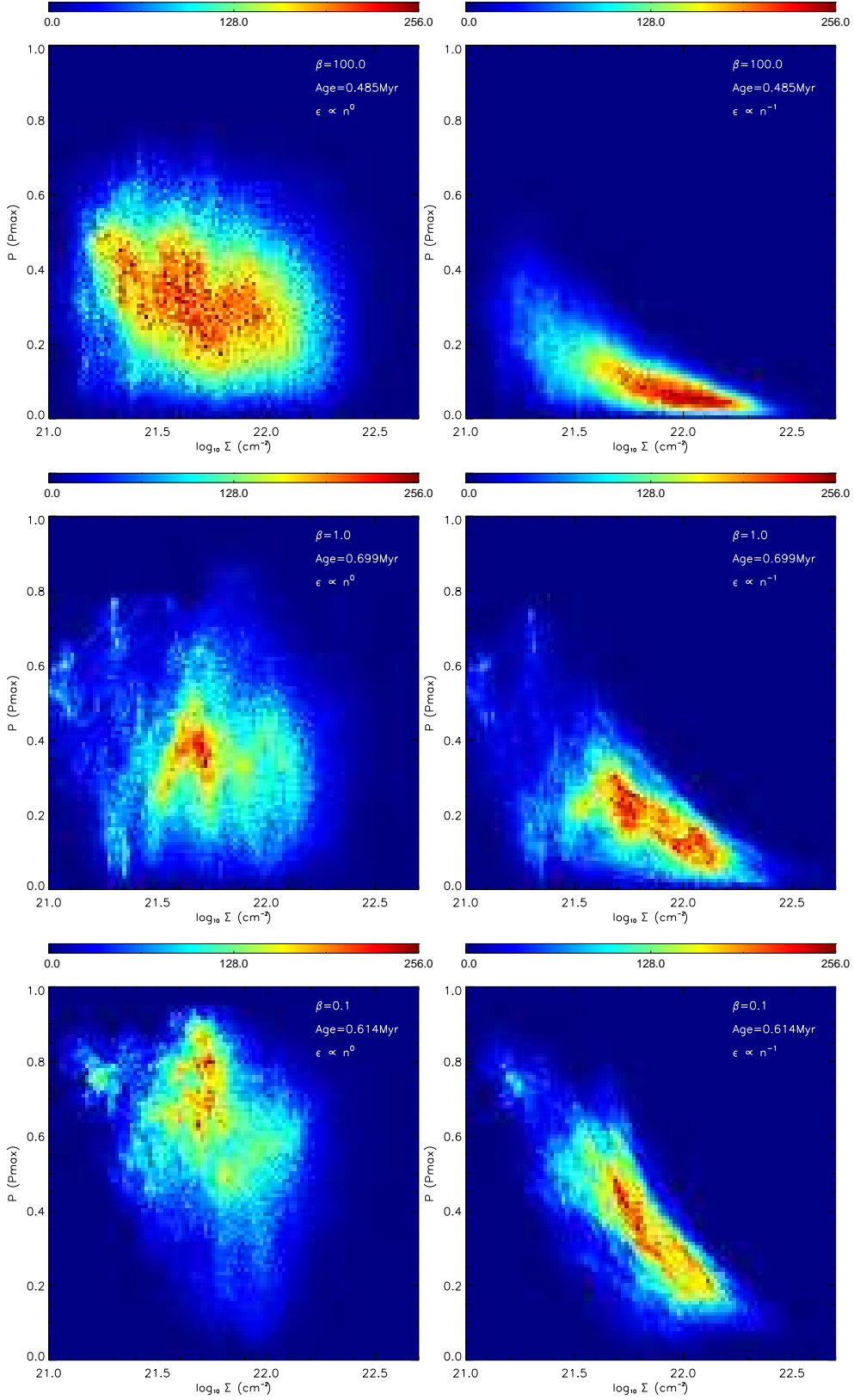


FIG. 11.— Polarization percentage P in units of maximum polarization percentage P_{max} as a function of column density obtained from the projections of the 3 simulations with uniform polarization efficiency $\epsilon = 1.0$. $P_{max} \sim 20\%$ is determined empirically from submillimeter diffuse Galactic dust emission (Benoît et al. 2004). These different distributions and the systematic behavior, especially on the right, offer diagnostics relating parameters in MHD simulations to observations.